Langmuir

Article

pubs.acs.org/Langmuir

# Structure of Multiresponsive Brush-Decorated Nanoparticles: A Combined Electrokinetic, DLS, and SANS Study

Jennifer R. S. Martin,[†,‡] Isabelle Bihannic,[†,‡] Catarina Santos,[§] José Paulo S. Farinha,[§] Bruno Demé,[∥] Frans A. M. Leermakers,[⊥] José P. Pinheiro,[†,‡] Elise Rotureau,[†,‡] and Jérôme F. L. Duval*[,†,‡]

[†]CNRS, LIEC (Laboratoire Interdisciplinaire des Environnements Continentaux), UMR7360, Vandoeuvre-lès-Nancy F-54501, France

[‡]Université de Lorraine, LIEC, UMR7360, Vandoeuvre-lès-Nancy F-54501, France

[§]Centro de Quimica Fisica Molecular and IN-Institute of Nanoscience and Nanotechnology, Instituto Superior Tecnico, University of Lisbon, 1049-001 Lisboa, Portugal

[∥]Institut Laue-Langevin (ILL), BP 156-X, F-38042 Grenoble Cedex, France

[⊥]Laboratory of Physical Chemistry and Colloid Science, Wageningen University and Research Center, Dreijenplein 8, 6703 HB Wageningen, The Netherlands

Supporting Information

**ABSTRACT:** Particles consisting of a glassy poly(methyl methacrylate) core (ca. 40 nm in radius) decorated with a poly(*N*-isopropylacrylamide) anionic corona are synthesized using either methacrylic acid (MA) or acrylic acid (AA) as reactive comonomers in the shell. The different reactivity ratios of MA and AA toward *N*-isopropylacrylamide originates p(MA-N) and p(N-AA) particles with carboxylate charges supposedly located, preferentially, in the close vicinity of the core and at the shell periphery, respectively. The corresponding swelling features of these nanoparticles are addressed over a broad range of pH values (4 to 7.5), $NaNO_3$ concentrations (3 to 200 mM), and temperatures (15 to 45 °C) by dynamic light scattering (DLS) and small angle neutron scattering (SANS). DLS shows that the swelling of the particle shells increases their thickness from ∼10 to 90 nm with decreasing temperature, ionic strength, or increasing pH, with the effect being more pronounced for p(N-AA) whose lower critical solution temperature is shifted to higher values compared to that of p(MA-N). Potentiometric titration and electrokinetic results further reflect the easier dissociation of carboxyl groups in p(N-AA) and a marked heterogeneous interfacial swelling of the latter with decreasing solution salt content. The DLS response of both particles is attributed to the multiresponsive nature of a peripheral dilute shell, while SANS only probes the presence of a quasi-solvent-free dense polymer layer, condensed on the core surface. The thickness of that layer slightly increases from ∼6 to 9.5 nm with increasing temperature from 15 to 45 °C (at 15 mM $NaNO_3$ and pH 5) due to the collapse of the outer dilute shell layer. Overall, results evidence a nonideal brush behavior of p(MA-N) and p(N-AA) and their microphase segregated shell structure, which supports some of the conclusions recently formulated from approximate self-consistent mean-field computations.

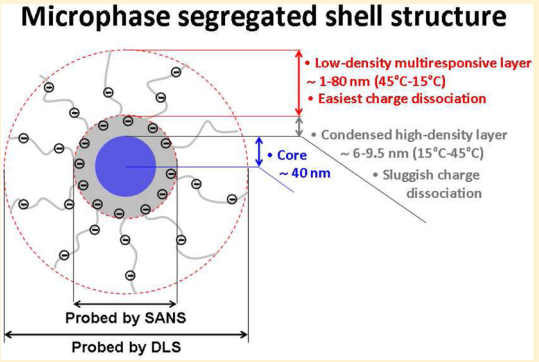


## 1. INTRODUCTION

Core−shell polymeric stimuli-responsive nanoparticles (RNPs) are a fascinating class of colloids due to their ability to change dimension, structure, chemical interactions, or aggregation state in direct response to external stimuli like temperature, pH, and ionic strength.[1−5] Because of their peculiar properties and the simplicity for obtaining controlled size distributions of such particles with different interfacial chemistries, they have been tested for a variety of applications ranging from sensors, medical diagnostics, drug delivery, and nanocatalysis to environmental remediation.[3,6,7] An attractive feature of these versatile particles is that they may be considered as relevant model systems for mimicking environmental nanocolloids that often possess a hard core supporting an adsorbed shell consisting of carboxylate-rich natural organic matter. As such, anionic RNPs are promising colloids for analyzing the binding of contaminants (like metal ions) to particles, under a broad range of physicochemical medium conditions affecting the size, structure, and lability of the formed metal complex.[8]

With the latter objective in mind, we recently synthesized core−shell particles composed of an ∼40 nm radius glassy poly(methyl methacrylate) (PMMA) core surrounded by an anionic shell of a copolymer of *N*-isopropylacrylamide (NIPAM) with either acrylic acid (AA) or methacrylic acid

**Received:** February 9, 2015
**Revised:** March 29, 2015
**Published:** April 3, 2015





DOI: 10.1021/acs.langmuir.5b00530
*Langmuir* 2015, 31, 4779−4790

(MA), using a two-stage starved-feed emulsion polymerization technique that produces highly monodisperse particles.[9] It is expected that the difference in reactivity of AA and MA comonomers toward NIPAM generates a difference in the distribution of carboxylate functional groups across the shell, resulting in p(N-AA) particles with charges preferentially located in the outer shell layer, and p(MA-N) particles with charges closer to the PMMA core.[9−11] In a first iteration, the particle shell was cross-linked with *N*,*N*′-methylene-bis-acrylamide to obtain a gel-like material whose swelling was reported on the basis of dynamic light scattering (DLS) measurements performed as a function of salt concentration, pH, and temperature.[9] In particular, the temperature response we found for the shell was characteristic of PNIPAM, which undergoes a reversible volume phase transition at a lower critical solution temperature (LCST) in the range 30 to 35 °C.[12,13] Because of functionalization with carboxylic groups, the volume phase transition also significantly depended on pH and ionic strength (~10 to 90 nm shell thickness), thus offering a remarkable range of operational conditions for tuning particle size and structure.

To attempt a theoretical reconstruction of the paramount effect of shell charges we observed on swelling behavior of particles with a cross-linked shell, we recently synthesized simpler, non-cross-linked p(MA-N) particles expectedly exhibiting a shell structure similar to that encountered for classical brush systems, which *a priori* facilitates comparison to theoretical prediction.[14] The swelling behavior of such particles was monitored as a function of temperature, pH, and salt concentration by DLS. Together with potentiometric titration data, the dependence of the polymer brush shell thickness on temperature, pH, and salinity was analyzed following the Scheutjens−Fleer self-consistent field (SF-SCF) approach.[14,15] Even for non-cross-linked p(MA-N) particles, seemingly simpler than the cross-linked systems investigated in ref 9, SF-SCF results suggested the existence of an unconventional microphase segregated shell structure, especially near the volume phase transition, where (i) most of the shell chains have collapsed in a dense region close to the core, and (ii) few charged chains significantly protrude from the core surface. On a quantitative level, significant discrepancies between theory and shell thickness measurements were observed, and a refined model, including inhomogeneous charge distribution along the chains and/or polydispersity in chains length, was not sufficient to fully rationalize the particle swelling features. Several reasons possibly explaining the failure of the SF-SCF approach to grasp the nonideal PNIPAM brush behavior were advanced, among them the neglect of 2D inhomogeneities in partially collapsed polyelectrolyte segments.[14]

This previous theoretical work on responsive polymer PNIPAM-based shells asks open-ended questions about the interrelationships between charge distribution in the shell, particle swelling behavior, and shell structure. Clearly, additional experimental work is required to challenge the theoretical conclusions drawn by Alves et al.[14] and to refine our understanding of the processes controlling at the molecular level the remarkable and peculiar behavior of PNIPAM particles in response to external stimuli. In particular, there is a need to collect information from techniques able to probe the structural and electrostatic characteristics of particle shell zones that differ according to their distance from the core surface. For that purpose, in this work, we systematically compare DLS, potentiometric titration, electrophoretic mobility, and small angle neutron scattering measurements versus temperature, pH, and salt concentration for non-cross-linked p(MA-N) and p(N-AA) particles. Results evidence (i) a spatial gradient in the dissociation constant of carboxylic groups across the particle shell due to the polyelectrolyte effect and changes in molecular environment of carboxylate charges, (ii) the existence of a poorly responsive dense and thin polymer layer close to the core, which confirms the microphase shell segregation previously suggested,[14] and (iii) a diffuse (heterogeneous) swelling of the outer periphery of the p(N-AA) shell with decreasing salt concentration. These experimental findings are thoroughly discussed in regard to the qualitative theoretical predictions given in a previous report.[14] They further help identifying the shortcomings of SF-SCF treatments[14,15] on p(MA-N) particles, thereby guiding further theoretical developments to capture the swelling behavior of these structured particulate shells.

## 2. MATERIALS AND METHODS

All routine reagents were used as received from the manufacturer without further purification: 0.0980 ± 0.060 M $HNO_3$, p.a., Riedel de Haen; 0.0976 ± 0.006 M NaOH, p.a., Merck; $NaNO_3$, p.a., Merck; and standard pH 4, 5, 6, and 7 buffers, Merck.

**2.1. Synthesis of Multiresponsive Core/Shell PNIPAM Particles.** Particles of interest in this work were synthesized following the protocol detailed elsewhere.[9,14] Briefly, particles were prepared by a two-stage shot emulsion copolymerization technique in ultrapure Milli-Q water, using the monomers methyl methacrylate (Aldrich, 99%, distilled under vacuum), *N*-isopropylacrylamide (NIPAM) (Acros, 99%, recrystallized in hexane), and either acrylic acid (AA) or methacrylic acid (MA) (both from Aldrich, 99%, distilled under vacuum). Potassium persulfate (Aldrich, 99% ACS reagent) served as initiator, and the surfactant was sodium dodecyl sulfate (Sigma, 99% GC grade). In a first step, the PMMA core was prepared by batch emulsion polymerization, and in a second stage, a mixture of NIPAM and MA (for p(MA-N)) or AA (for p(N-AA)) was added in three shots, 10 min apart, to the reactive medium at 70 °C, to form the shell around the PMMA core. The particles were cleaned by dialysis against Milli-Q water using a Spectra/Por membrane (MWCO of 6−8 kDa), renewing the water bath twice a day for 1 week.

**2.2. Dynamic Light Scattering (DLS).** Particle diffusion coefficients were measured by DLS using a Zetasizer Nano ZS instrument (He−Ne red laser (633 nm), Malvern Instruments). The apparatus is equipped with a temperature-controlled quartz Suprasil measurement cell, an automatic laser attenuator, and an avalanche photodiode detector. The position of the latter is located 173° relative to the laser source, which ensures backscattering detection. Experiments were driven by the Dispersion Technology software from Malvern Instruments. Particles were dispersed at a final volume fraction of $5 \times 10^{-3}$% in 3 mM to 200 mM $NaNO_3$ electrolyte solution with pH in the range 4 to 7.5. Solution pH and salinity were fixed after the addition of appropriate aliquots of 0.1 M NaOH, 0.1 M $HNO_3$, and 1 M $NaNO_3$ solutions in ultrapure Milli-Q water. Prior to measurements under given pH and salt concentration conditions, particle dispersions were systematically pre-equilibrated at the desired temperature (15 to 45 °C) for a period of at least 40 min. Particle diffusion coefficients were derived from analysis of the obtained intensity autocorrelation function. In a first approximation, the corresponding monomodal (intensity-based) distributions in the (hydrodynamic) size of equivalent hard spheres were evaluated on the basis of the Stokes−Einstein equation. For swelling data analysis purposes, DLS measurements were also performed on $5 \times 10^{-3}$ vol % dispersions of particles devoid of the shell component, providing a 42 ± 1 nm intensity-average core radius, in line with the result given in ref 9.

**2.3. Potentiometric Titrations and Electrophoretic Mobility Measurements.** Details on the titration procedure adopted for the non-cross-linked p(MA-N) and p(N-AA) particles synthesized in this


DOI: 10.1021/acs.langmuir.5b00530
*Langmuir* 2015, 31, 4779−4790

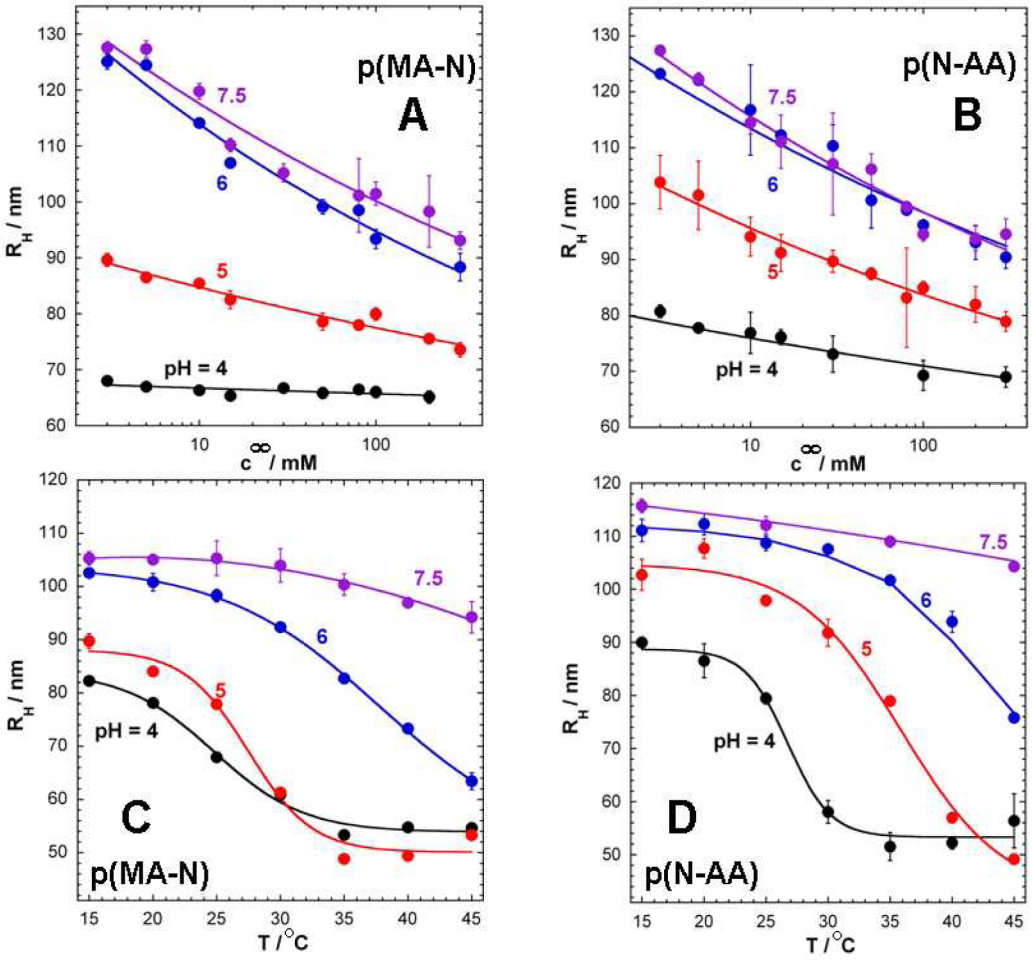


**Figure 1.** Hydrodynamic size radius $R_H$ measured by dynamic light scattering (DLS) as a function of pH, $NaNO_3$ electrolyte concentration (denoted as $c^\infty$), and temperature for p(MA-N) (panels A,C) and p(N-AA) particles (panels B,D). (A,B) $T$ = 25 °C. (C,D) $c^\infty$ = 15 mM and pH 5. Symbols: experimental data. Solid lines in A and B: fit of data according to the power-law $R_H \propto a + (c^\infty)^{-\beta}$. Solid lines in C and D: lines to guide the eye.

work are available elsewhere.[14] Briefly, after calibration of the pH electrode, a blank subtraction procedure was applied. To obtain reference blank values, pH was initially set to 3.0, and the medium was titrated up to pH 11 by successive additions of 5 $\mu$L of 0.1 M NaOH, and back-titration to pH 3.5 was conducted by successive additions of 5 $\mu$L of 0.1 M $HNO_3$. For the second and third back and forth blank titrations, the procedure was repeated with the appropriate additions of 1 M $NaNO_3$ to set the ionic strength at 3 mM, 15 mM, and 100 mM. For titrations of dispersions containing p(MA-N) or p(N-AA) particles, the adopted procedure was identical to that described above for the blank titration except that the initial 20 mL solution contained 0.15% volume fraction of particles dispersed in 3 mM, 15 mM, and 100 mM $NaNO_3$. The blanks were then subtracted from the titration data in order to estimate the pH- and salt concentration-dependent particle charge content. The potentiometric measurements were performed using a Mettler-Toledo T90 system with four 1 mL-autoburetes and a Mettler-Toledo combined pH glass electrode DGi102 mini. The system was constantly under nitrogen purging. Mettler-Toledo LabX titration software was used to control the apparatus.

Using the Zetasizer Nano ZS instrument mentioned above (section 2.2), the particles' electrophoretic mobility ($5 \times 10^{-3}$ vol % dispersions) was measured as a function of pH, salt concentration, and temperature under the conditions adopted for the DLS measurements. Electrophoretic mobility was determined from phase analysis light scattering (PALS), which allows evaluation of particle velocity from the phase shift between light scattered by moving particles under application of a constant direct-current electric field and a reference beam.

**2.4. Small Angle Neutron-Scattering (SANS).** SANS experiments were performed at the low momentum transfer small-angle neutron scattering instrument D11 at the Institut Laue-Langevin (ILL-Grenoble, France). Data were collected at a neutron wavelength $\lambda$ = 8 Å, using 4 sample-to-detector distances (28 m, 12 m, 4 m, and 1.2 m) resulting in the $1.2 \times 10^{-3}$ to 0.38 $Å^{-1}$ range for the accessible momentum transfer $q$ defined by $q = 4\pi \sin(2\theta)/\lambda$ with $\theta$ the scattering angle. Data were corrected for electronic noise, detector efficiency, and scattering contribution from the empty cell. Following the classical integration procedure, all two-dimensional scattering patterns were radially averaged to get a 1D plot of the scattered intensity versus $q$. The full data treatment was carried out using LAMP software provided by ILL. Measurements were performed on 1% (w/w) p(MA-N) and p(N-AA) dispersion samples with temperature in the range 15 to 45 °C at pH 5 and 15 mM $NaNO_3$ concentration. These conditions correspond to those where the dependence of the hydrodynamic particle radius on temperature, as determined by DLS, is most pronounced. SANS measurements were performed using $D_2O$ as solvent in order to minimize the incoherent signal from $H_2O$. For adjustment of the solution pH, we used the relationship pD = pH + 0.41.[16] The procedure followed for the preparation of the samples used in the SANS experiments consisted of cleaning of the p(MA-N) and p(N-AA) particle dispersions, as detailed in section 2.1. Then, the exchange of $H_2O$ for $D_2O$ was achieved by dialysis for 10 days adopting the dialysis protocol mentioned for the cleaning stage in section 2.1.



DOI: 10.1021/acs.langmuir.5b00530
*Langmuir* 2015, 31, 4779−4790

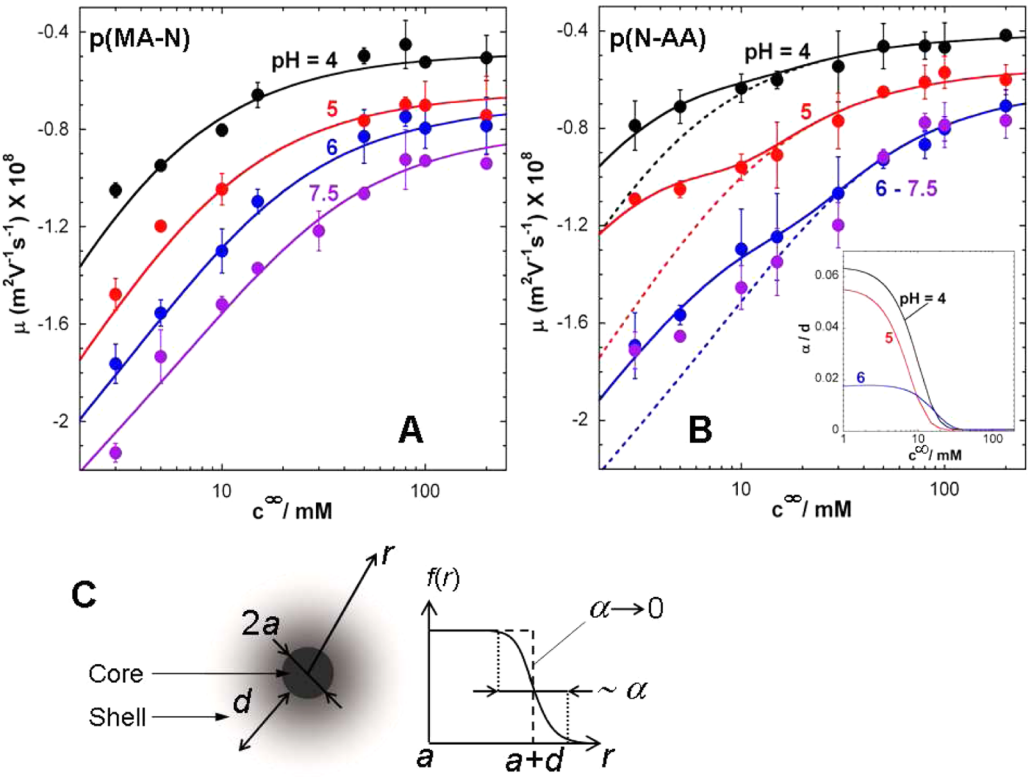


**Figure 2.** Dependence of the electrophoretic mobility $\mu$ of p(MA-N) and p(N-AA) particles (panels A and B, respectively) on $NaNO_3$ electrolyte concentration at various pH values (indicated). Symbols: experimental data. Solid lines in A and B: predictions from the theory for electrokinetics of diffuse soft particles[21,22] applied in the limit $\alpha \to 0$. Dotted lines (panel B): predictions with the adjustment of $\alpha$ as detailed in the inset of panel C where the diffusiveness $\alpha/d$ of the shell/solution interphase is given with $d$ pertaining to the shell thickness derived from Figure 1B. Panel C: schematic representation of a soft diffuse core−shell particle with $f(r)$ the radial distribution of chains density at the shell/solution interphase.[21,22] For the sake of clarity, carboxylate and ionic charges are not represented. See text for further details (section 3.2).

## 3. RESULTS AND DISCUSSION

**3.1. Comparison between Multiresponsive p(MA-N) and p(N-AA) Swelling Behavior.** *3.1.1. Size Dependence on pH and Electrolyte Concentration.* Figure 1A and B show the variations of p(MA-N) and p(N-AA) hydrodynamic radii $R_H$, respectively, with increasing electrolyte concentration from $c^\infty$ = 3 mM to 200 mM at room temperature (25 °C) and pH 4, 5, 6, and 7.5. Under such conditions, $R_H$ of both particle types decreases in the range ∼130 nm to ∼70 nm with increasing $c^\infty$ due to the screening of carboxylate shell charges and that of their repulsive electrostatic interactions. Upon increase of solution pH at fixed $c^\infty$, the carboxylic groups located in the particle shell deprotonate, the amount of negative charges increases, and their repulsive interactions lead to particle shell expansion, which is manifested by an increase of $R_H$. At pH 4 and 5, it is noteworthy that the extent of particle charge screening and, therewith, the magnitude of shell collapse with increasing $c^\infty$, is most pronounced for p(N-AA) particles. This may be explained by the preferential location of the carboxylate groups at the outer shell periphery of p(N-AA), which could facilitate their shielding by ions from the background electrolyte. Alternatively, the dissociation properties of the carboxylic groups may depend on their preferential location in the vicinity of the particle core (case expected for p(MA-N) particles) or at the outer shell region (situation for p(N-AA) particles). *In fine*, this would result in differentiated swelling/collapse response to changes in solution pH.

As detailed below, charge titrations, electrokinetics, and pH/temperature-dependent particle swelling support the existence of such a difference between deprotonation features of carboxylic groups in p(MA-N) and p(N-AA) shells. Unlike p(MA-N), p(N-AA) exhibits, within experimental uncertainty, identical swelling behavior at pH 6 and 7.5, which suggests that complete dissociation of carboxylic groups in the p(N-AA) shell is reached at pH $\geq$ 6. On a quantitative level, the brush thickness $R_H - a$ decreases with $c^\infty$ according to the power law $R_H - a \propto (c^\infty)^{-\beta}$ ($a$ is the core radius; $a$ = 42 nm; see section 2.2) with $\beta \sim 0.07$ and 0.10−0.12 for p(N-AA) at pH 4 and 5−7.5, respectively, and $\beta \sim 0.02$, 0.08, and 0.11−0.13 for p(MA-N) at pH 4, 5, and 6−7.5, respectively. While this power law is in qualitative agreement with analytical scaling theory for weak polyelectrolyte brushes in the "salted brush regime",[17] we see comparatively a weaker power-dependence of the brush thickness on $c^\infty$ than the classically predicted $(c^\infty)^{-1/3}$ dependence. Reasons for this deviation are provided in Supporting Information (Part I, Figure S1) where we give typical self-consistent field modeling of brush height as a function of solution ionic strength and pH.

*3.1.2. Size Dependence on Temperature.* Figure 1C and D display the dependence of particle size $R_H$ on temperature $T$ at $c^\infty$ = 15 mM and pH 5. The data highlight the temperature-driven volume-phase transition expected for PNIPAM copolymers, with a decrease of $R_H$ upon increasing $T$. This phase transition results from the entropically driven aggregation of the polymer segments due to attractive interactions between hydrophobic isopropyl groups that overcome water-amide groups hydrogen bonding at temperatures higher than the so-called lower critical solution temperature (LCST).[18] At fixed



DOI: 10.1021/acs.langmuir.5b00530
Langmuir 2015, 31, 4779−4790

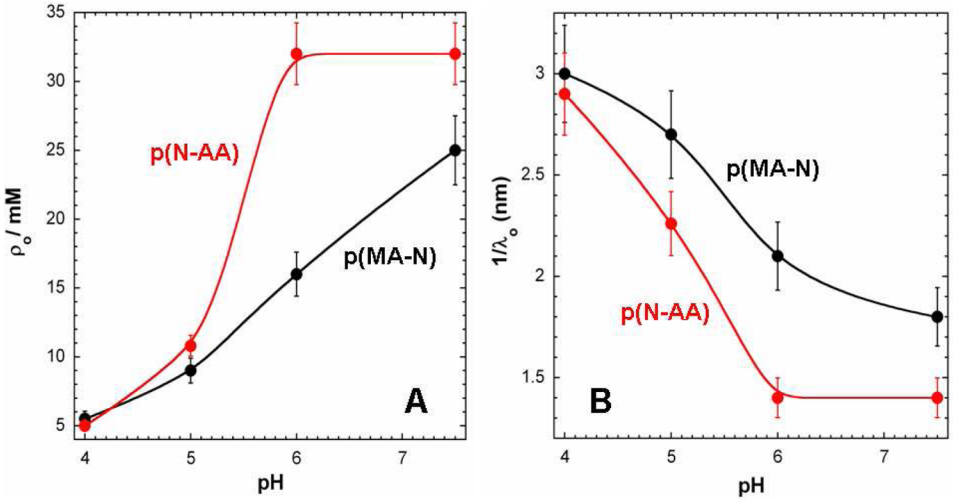


**Figure 3.** (A) Density $\rho_o$ of charges in the particle shell and (B) characteristic penetration length $1/\lambda_o$ derived from theoretical analysis of the electrolyte concentration-dependent electrokinetic data collected in Figure 2 for p(MA-N) and p(N-AA) particles (indicated). $\rho_o$ is expressed in minus the equivalent concentration of elementary charges.

temperature, $R_H$ increases with pH for the reasons already evoked in Figure 1A and B. With increasing pH, the LCST is shifted to higher values, which is typical for multiresponsive charged polymer systems.[9,13,19] Basically, this shift stems from the balance between a favored hydration of the polymer chains with increasing pH (due to the accompanying increase in shell charges) and the reduced chain hydration at sufficiently large $T$. In detail, the LCST of p(N-AA) increases from 27 to 36 °C with increasing pH from 4 to 5, while the LCST of p(MA-N) remains close to 27 °C in this pH window. Complete p(MA-N) shell collapse is achieved for $T \geq 35$ °C at pH 4 and 5, while that of the p(N-AA) shell is reached for $T \geq 35$ °C and $T \geq 40$ °C at pH 4 and 5, respectively. At higher pH values, the transition between expanded- and collapsed-shell state cannot be identified within the temperature range tested in this work, and collapsed p(N-AA) and p(MA-N) shells are obviously obtained for temperatures that well exceed 45 °C. The distinct pH- and temperature-dependent LCST found for p(MA-N) and p(N-AA) particles conforms to the idea that the dissociation properties of the carboxylic groups are different for these two systems, recalling that, from chemical synthesis, the total amount of charges is expectedly the same.

**3.2. Electrokinetic and Protolytic Properties of p(MA-N) and p(N-AA) Particles.** *3.2.1. Electrokinetics.* To quantitatively address the electrostatic properties of p(MA-N) and p(N-AA) particles, their electrophoretic mobility $\mu$ was measured at different pH values, at room temperature (25 °C), as a function of $NaNO_3$ electrolyte concentration $c^\infty$ (Figure 2A and B).

Overall, the electrokinetic response of both systems is typically that expected for soft particles with a water-permeable shell.[20] Namely, at a given pH, $|\mu|$ decreases with increasing $c^\infty$ due to enhanced screening of particle charges, and it reaches asymptotically a constant nonzero plateau value at sufficiently large electrolyte concentrations (>100 mM). This peculiar asymptotic mobility behavior at $c^\infty \to \infty$ reflects the ability of the electroosmotic flow to penetrate the particle shell and probe the therein distributed electrokinetically active carboxylate charges.[20,21] Under all conditions examined here, $\mu$ is negative, in line with the sign of the carboxylate charges in p(MA-N) and p(N-AA). At a given salt concentration, the mobility $\mu$ increases in absolute value with pH as a result of the deprotonation of the carboxylic groups. In agreement with Figure 1B, the electrokinetic properties of p(N-AA) particles are basically identical at pH 6 and 7.5, which supports the hypothesis that complete dissociation of carboxylic groups is achieved for pH ≥ 6 in the p(N-AA) shell. In contrast, clearly distinct electrokinetic profiles are measured for p(MA-N) at pH 6 and pH 7.5, which confirms that full dissociation of carboxylic groups is not achieved under such pH conditions for p(MA-N) where charges are significantly embedded within the shell component. This finding is again consistent with the distinct swelling response of p(MA-N) measured at pH 6 and 7.5 with changing electrolyte concentration (Figure 1A).

*3.2.2. Framework of Electrokinetic Modeling.* On a quantitative level, the $c^\infty$-dependent mobility $\mu$ was analyzed at pH 4, 5, 6, and 7.5 using the theoretical formalism developed by Duval et al.[22] for the electrophoretic mobility of soft diffuse spherical particles (Figure 2C). Unlike the approximate mobility expression originally formulated by Ohshima for large, homogeneous soft particles under Donnan conditions,[20] the theory allows for electrophoretic mobility evaluation without any limitations on soft particle size and on the charge density it carries. It takes into account the effects of electric double layer relaxation/polarization on electrophoresis, and it further includes the impact of radial distribution of polymer chain density across the soft interface. The model is based on the representation by Debye–Bueche and Brinkman for the friction forces exerted by the particle shell on hydrodynamic flow.[23] Using a collocation algorithm,[24] the particle mobility is computed from the rigorous numerical solution of the coupled (i) (nonlinearized) Poisson–Boltzmann equation, (ii) extended form of the Navier–Stokes equation, (iii) governing equations for intra- and extra-particulate ion transports, and (iv) continuity equations for fluid and ion fluxes. The reader is referred to refs 21 and 22 and references therein for further details. Briefly, assuming homogeneous distribution of fixed (immobile) charges in the particle shell, two key variables are required for data modeling: the density $\rho_o$ of charges in the particle shell and the characteristic penetration length $1/\lambda_o$ of the electroosmotic flow in the shell. For cases where there is a diffuse distribution of polymer chains density from bulk value



DOI: 10.1021/acs.langmuir.5b00530
*Langmuir* 2015, 31, 4779–4790

to zero outside the shell (Figure 2C), the analysis requires the further specification of the segment density distribution $f(r)$ across the particle shell compartment, with $r$ the radial position.[21,22] As a first approximation, a tanh-like function may be adopted for the radial dependence of $f$ that involves, then, a key length scale, denoted $\alpha$, reflecting the sharpness in chains density distribution at the particle shell/solution interphase,[21,22] as illustrated in Figure 2C. Finally, it is stressed that the electrokinetic modeling is based on a smeared-out representation of the shell according to the angular coordinate, which may be a severe approximation for particulate systems whose dilute outer shell consists of protruding chains that are far apart from each other (at least with a separation distance much larger than the Debye length). For the lack of better theory, we proceed on the following on the basis of the above formalism. As later discussed, it correctly captures the basic connections between the expected charges location in the shell and the shell electrohydrodynamic properties.

*3.2.3. Quantitative Interpretation of p(MA-N) and p(N-AA) Electrokinetics.* For modeling purposes, the particle core radius $a$ and the shell thickness $d$ are required quantities. The former is known here from DLS measurements ($a$ = 42 nm; see section 2.2), and the dependence of the latter on $NaNO_3$ concentration and solution pH is simply derived from the corresponding core−shell particle size obtained by DLS (Figure 1) and corrected for the size of the core. As a first approach, we attempted a reconstruction of the mobility data with $\alpha \to 0$, thus assuming a step-function like density distribution in the particle shell. This representation is legitimate, in particular, in the thin double layer limit reached at sufficiently large electrolyte concentrations where electrostatic interactions between carboxylate charges are screened to such an extent that $\alpha/d \ll 1$.[21,22] The comparison between experiments and theory is given in Figure 2A for p(MA-N) particles. The corresponding dependence of $\mu$ on $c^\infty$ and pH is remarkably well reproduced by the theory, requiring only the fitting of the parameters $\rho_o$ and $1/\lambda_o$ with changing pH, as detailed in Figure 3A and B, respectively. Following the deprotonation of the carboxylic groups, $\rho_o$ (expressed in minus the equivalent concentration of elementary charges) gradually increases from 5 mM to 25 mM upon increasing pH from 4 to 7.5. The complete dissociation of the carboxylic groups probed by electrokinetics (see discussion below) is, however, not achieved as $\rho_o$ does not reach a plateau value at large pH. The flow penetration length $1/\lambda_o$ further decreases from 3 to 1.8 nm with pH in the range 4 to 7.5. This trend basically reflects the pH-mediated swelling of the particle shell where protruding polymer chains increasingly suppress the electroosmotic flow in the direct shell vicinity, leading to a decrease in $1/\lambda_o$. Under the swelling conditions detailed in Figure 1A, we verified *a posteriori* that the mobility $\mu$ of p(MA-N) particles remains independent of the shell thickness $d$. This is simply because $d$ is significantly larger than the key physical length scales of the electrohydrodynamic problem, namely, the reciprocal of the hydrodynamic softness, $1/\lambda_o$, and the electric double layer thickness, $1/\kappa$.[21,22] The independence of $\mu$ on $d$ was demonstrated long ago by Ohshima in the derivation of his famous analytical expression for the mobility of soft particles satisfying $\lambda_o d \gg 1$ and $\kappa d \gg 1$.[20] Application of this simple expression is, however, correct provided that the particle core surface may be further regarded as planar for the evaluation of the relevant electrostatic and hydrodynamic flow fields, i.e., $a \to \infty$. This latter condition is not satisfied for the particles examined in this work in the range 3 mM to 200 mM salt concentration, a conclusion derived from comparing the theoretical data of Figure 2 with mobility predictions obtained from Ohshima's approximate analytical theory (not shown). Finally, it is emphasized that $\mu$ reflects the electrohydrodynamic properties of an outer particle shell region whose (few-nm) thickness is a complex function of $1/\kappa$ and $1/\lambda_o$: this electrokinetically active interphasial zone where the local electroosmotic flow velocity is not zero defines the amount of shell charges effectively probed by the flow.[21] Analogy may be drawn for other electrokinetic phenomena on soft interphases, e.g., streaming current at polyelectrolyte multilayers/solution interphase.[25]

Figure 2B reports the analysis of p(N-AA) electrokinetics, following the same strategy as that detailed above for p(MA-N). For electrolyte concentrations $c^\infty \geq 20$ mM, the theory adequately reproduces the dependence of $\mu$ on pH and $c^\infty$ with $\alpha \to 0$. The required adjustment of $\rho_o$ and $1/\lambda_o$ with varying pH is given in Figure 3. Unlike p(MA-N), $\rho_o$ now increases with pH before reaching a plateau value at pH 6 that reflects the complete dissociation of the carboxylic groups distributed within the shell zone effectively probed by the electroosmotic flow. In addition, $\rho_o$ is similar at pH 4 for p(N-AA) and p(MA-N), but it is systematically higher (in absolute value) in the shell of the former particle type as compared to that of p(MA-N). Similarly to p(MA-N), $1/\lambda_o$ for p(N-AA) decreases with increasing pH as a result of shell swelling. The magnitude of this decrease in $1/\lambda_o$ is, however, larger for p(N-AA) particles, which is consistent with the larger shell expansion obtained for this particle type under fixed salt concentration conditions (Figure 1B). For electrolyte concentrations $c^\infty < 20$ mM, the theoretical simulations with $\alpha \to 0$ systematically overestimate the mobility magnitude $|\mu|$ of p(N-AA) (see dotted lines in Figure 2B). This discrepancy between theory and experiments is classically observed at low $c^\infty$ for soft diffuse interphases characterized by a finite nonzero spatial gradient in chain density distribution.[21,22] Basically, with decreasing salt concentration, there is an heterogeneous swelling of the chains at the periphery of the p(N-AA) shell, which is materialized by an increase of the length scale $\alpha$ (inset Figure 2B). This leads to an additional increase in flow suppression extent due to the friction exerted by the most protruding chains, thereby lowering the magnitude of the particles mobility compared to the situation where chains swelling is homogeneous (see difference between dotted and solid lines in Figure 2B). Stated differently, the introduction of a diffuse shell interphase via increasing $\alpha$ corrects for the aforementioned discrepancy obtained at low $c^\infty$ if reasoning in terms of homogeneous chains density distribution at the outer shell region. We verified that the higher is $c^\infty$, the lesser is the impact of $\alpha$ on $\mu$, in agreement with previous theoretical conclusions.[21] Finally, it is observed that the degree $\alpha/d$ of shell interphase diffuseness slightly decreases with pH at fixed $c^\infty$ (inset Figure 2B). This counterintuitive result probably originates from the swelling of charged chains located in a hydrodynamically screened shell zone inaccessible by the electroosmotic flow.

*3.2.4. Discussion.* At this stage of the analysis, it is clear that the electrokinetic charge estimated for p(N-AA) is higher, in magnitude, than that in p(MA-N) shell (Figure 3A), except at pH 4−5 where deprotonation of carboxylic groups is not significant. This finding supports the preferential location of carboxylate p(N-AA) charges at the outer particle shell periphery where the electroosmotic flow field is most



DOI: 10.1021/acs.langmuir.5b00530
*Langmuir* 2015, 31, 4779−4790

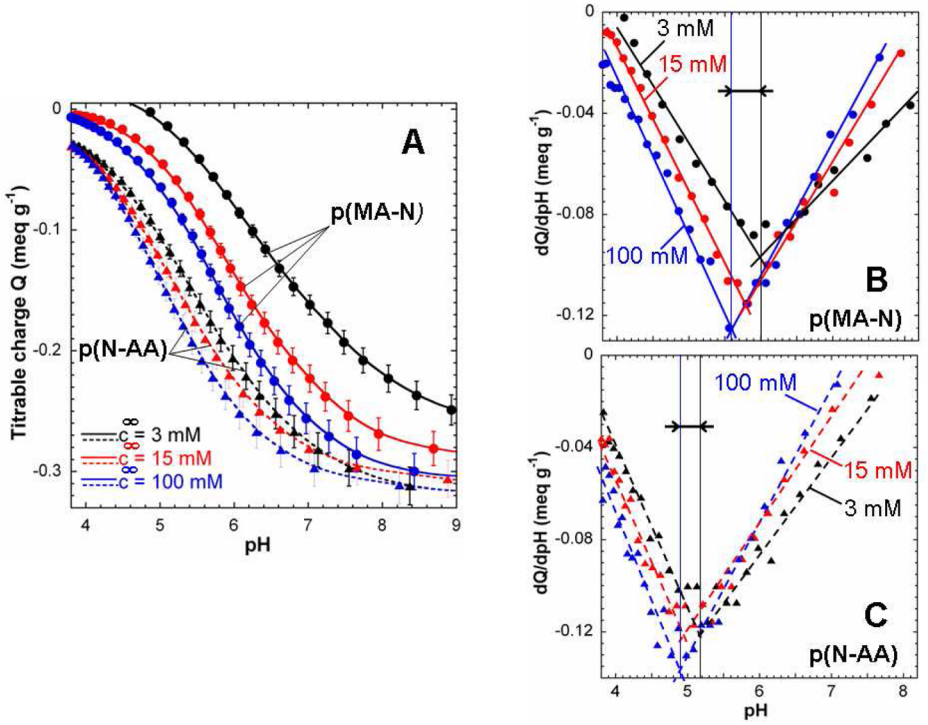


**Figure 4.** (A) Evolution of the amount of titrable charges $Q$ in meq $g^{-1}$ with pH and $NaNO_3$ electrolyte concentration (indicated) for p(MA-N) and p(N-AA) particles (indicated). (B) Representation of the derivative $dQ/dpH$ for p(MA-N) (B) and p(N-AA) (C) as a function of pH at 3 mM, 15 mM, and 100 mM $NaNO_3$ electrolyte concentration (indicated). In panels B and C, the vertical lines materialize the polyelectrolyte effect (i.e., the shift of the apparent dissociation constant with changing electrolyte concentration), while solid (B) and dotted (C) lines are only guides to the eye.

significant. For both p(MA-N) and p(N-AA), pH-mediated shell swelling is accompanied by a decrease of $1/\lambda_o$, which translates the enhanced friction exerted by the protruding chains on the flow. The larger is the shell expansion, the most pronounced is this effect (Figure 3B), in line with the respective swelling behavior measured by DLS for p(MA-N) and p(N-AA) (Figure 1A and B, respectively). Figure 2A further shows that carboxylic groups in the electrokinetically active p(N-AA) shell region undergo an easier dissociation with increasing pH as compared with charges in the outer p(MA-N) shell where complete carboxylic group dissociation is not achieved in the pH range 4 to 7.5 (Figure 3A). It is known that the protonation/deprotonation process of ionogenic groups is governed by the polyelectrolyte effect and is further sensitive to the hydrophobic/hydrophilic balance of their close molecular environment.[26,27] The p(MA-N) charges that significantly recede within the shell are likely exposed to hydrophobic patches and/or they experience stronger electrostatic fields, thus resulting in their retarded dissociation with pH.

The differentiated dissociation properties of carboxylic groups in p(MA-N) and p(N-AA) shells are confirmed by potentiometric titrations (Figure 4A) that show the sluggish dissociation of p(MA-N) carboxylic groups compared to that of the p(N-AA) shell charges. Titration data further highlight that the polyelectrolyte effect, marked by an increase of the (apparent) dissociation constant $pK_a$ of carboxylic groups with decreasing electrolyte concentration $c^\infty$,[28] is basically identical for p(MA-N) and p(N-AA). Indeed, quantitatively, a derivation of the titration curves with respect to pH (Figure 4B and C) shows that $pK_a$ increases by 0.3 units (~4.9 to 5.2) for carboxylic groups in p(N-AA) with decreasing $c^\infty$ from 100 mM to 3 mM, and $pK_a$ increases by 0.4 units (5.6 to 6) in this salinity range for carboxylic groups in p(MA-N). Then, the difference in $pK_a$ values between carboxylate groups in p(N-AA) and p(MA-N) shells is probably the only result of their different molecular environments, as mentioned above. Adopting the simplistic Langmuirian deprotonation function $\rho_o/\rho_o^{max} = (1 + 10^{pK_a - pH})^{-1}$ with $\rho_o^{max} = 32$ mM (see Figure 3A), we obtain from electrokinetics $pK_a \sim 5.3$ and $pK_a \sim 6$ for p(N-AA) and p(MA-N), respectively, which satisfactorily compares with the apparent $pK_a$ values estimated above from titration experiments. Finally, the total amount of titrable charges obtained at 100 mM and large pH in p(N-AA) and p(MA-N) is ca. 0.3 mequiv $g^{-1}$ that converts into a maximum charge density $\rho_o^{max}$ of 300 mM, i.e., ca. 10 times higher than the maximum charge density evaluated from electrokinetics. Such a discrepancy between electrokinetic and titrable charges is well documented in the literature,[29] and it is attributed to the restricted shell interphasial region effectively probed by electrokinetics. For the systems of interest here, 90% of the charges are not "detected" from electrophoretic mobility analysis. These charges are therefore located within an electrokinetically inactive shell zone that is sufficiently away from the shell/solution interphase.

Finally, electrophoretic mobilities of p(N-AA) particles measured at different temperatures under fixed pH and salinity conditions are reported in Supporting Information (Part II, Figure S2). Their quantitative interpretation, with accounts of the tabulated temperature-dependent water dielectric permittivity, viscosity,[30,31] and ionic limiting conductivities of $Na^+$ and $NO_3^-$,[32,33] supports the consistency of the above electrokinetic modeling performed as a function of pH and salt concentration (Figure 2B).

**3.3. Small Angle Neutron Scattering (SANS).** *3.3.1. Experimental Data.* To further access the structural organization of the shell in p(N-AA) and p(MA-N), SANS curves were



DOI: 10.1021/acs.langmuir.5b00530
*Langmuir* 2015, 31, 4779−4790

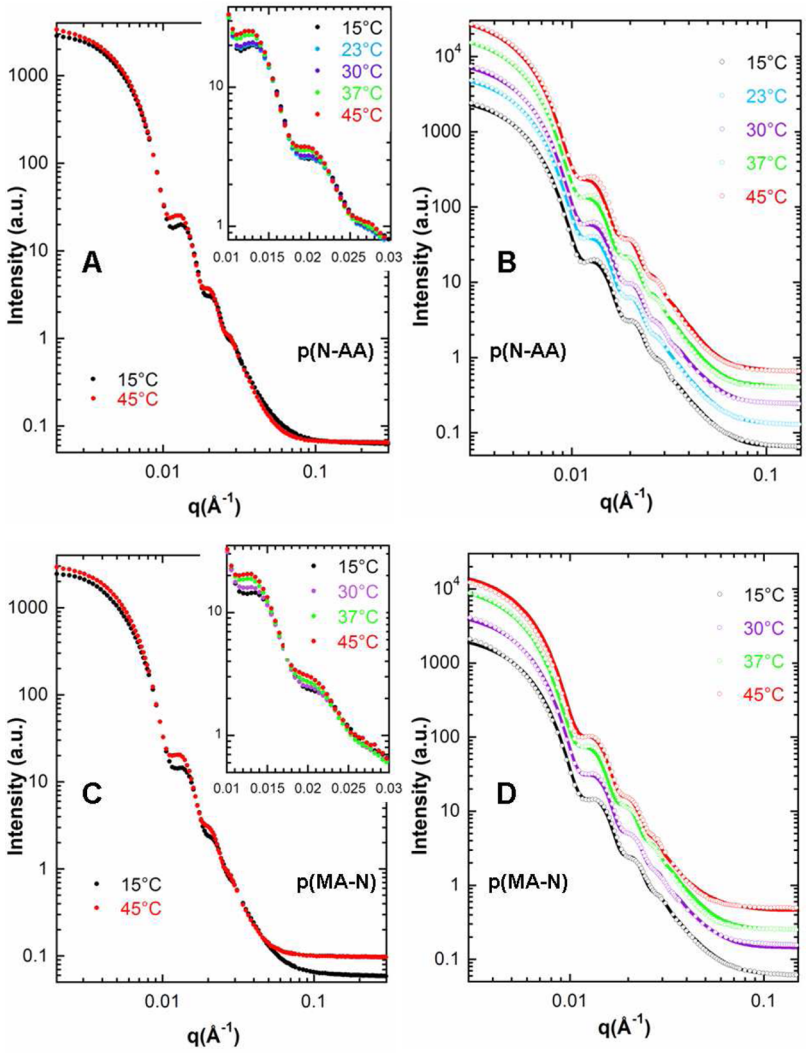


**Figure 5.** Small angle neutron scattering patterns measured for p(N-AA) (panels A,B) and p(MA-N) particles (panels C,D) at various temperatures (indicated), $c^{\infty}$ = 15 mM and pH 5. Symbols (open and filled circles): experimental data points. Solid lines in panels B and D: theoretical fit obtained as detailed in Supporting Information (Part III). While panels A and C show the full $q$-dependence of the scattered intensity $I$ at the extremes $T$ = 15 and 45 °C, insets provide a zoomed view of the subtle changes of $I(q)$ with varying temperature in the range 15 °C−45 °C. For the sake of clarity, the $I(q)$ curves measured at different temperatures were vertically shifted in panels B and D to facilitate comparison with theory.

recorded on both systems at various temperatures, $c^{\infty}$ = 15 mM and pH 5 (see experimental details in section 2.4).[34] These conditions correspond to those leading to the most significant variation in particle hydrodynamic radius $R_H$ with changing temperature, as shown in Figures 1C and D. The results obtained for p(N-AA) and p(MA-N) are collected in Figure 5A,B and C,D, respectively. At a given temperature, the overall decrease in intensity with increasing the momentum transfer $q$ and the presence of marked oscillations qualitatively correspond to the behavior expected from the form factor expression of relatively monodisperse particles with spherical geometry. For both p(N-AA) and p(MA-N) particle types, the intensity minima of the oscillations are shifted to smaller $q$ values with increasing temperature, suggesting an overall few nm increase of the particle size with increasing $T$. This finding contradicts *a priori* the shell collapse measured by DLS under such temperature conditions (Figures 1C,D). Solid explanation for this puzzling and remarkable result will be detailed below from quantitative data interpretation. At fixed temperature, the oscillations are better marked for p(N-AA), and the intensity minima are located at slightly lower $q$ positions compared to those for p(MA-N) (Figure S3 in Supporting Information, Part III). In order to relate these small but experimentally meaningful temperature-dependent changes of the SANS curves to the corresponding modulations of the particle shell structure, we now proceed to data analysis using SasView software (http://www.sasview.org/).

*3.3.2. Discussion.* Figure 5B and D show the successful reconstruction of the temperature-dependent SANS curves of p(MA-N) and p(N-AA) core−shell particles, respectively, on the basis of the constrained fitting procedure extensively detailed in Supporting Information (Part III). The analysis is based on the classical expression for the dependence of the scattered intensity $I$ on momentum transfer $q$, as originally derived by Guinier and Fournet for core−shell particles.[35,36] The values found for the scattering length density of the shell, $SLD_{shell}$, and for the shell thickness, $d$, are collected in Table 1 for both systems at $T$ = 15 °C, 23 °C, 30 °C, 37 °C, and 45 °C ($c^{\infty}$ = 15 mM, pH 5). Table S1 in Supporting Information (Part III) further summarizes all other parameter values



DOI: 10.1021/acs.langmuir.5b00530
*Langmuir* 2015, 31, 4779−4790

Table 1. Summary of the Core and Shell Sizes Derived for p(N-AA) and p(MA-N) Particles from SANS Data Modeling at Different Temperatures[a]

| sample | p(N-AA) 15 °C | p(N-AA) 23 °C | p(N-AA) 30 °C | p(N-AA) 37 °C | p(N-AA) 45 °C |
|---|---|---|---|---|---|
| core radius $a$ (nm) | 36.7 | 36.7 | 36.7 | 36.7 | 36.7 |
| $SLD_{shell}$ ($cm^{-2}$) | $7.1 \times 10^9$ | $8.1 \times 10^9$ | $7.8 \times 10^9$ | $7.8 \times 10^9$ | $7.0 \times 10^9$ |
| shell thickness $d$ (nm) | 6.8 ± 2.3 | 7.5 ± 2.5 | 7.4 ± 2.5 | 9 ± 2.6 | 9.4 ± 2.6 |
| $\varphi$ | 1.00 | 0.98 | 0.99 | 0.99 | 1.00 |
| DLS core−shell radius (nm) (volume-average) | 103.5 | 97.5 | 90.5 | 70 | 46.5 |
| SANS core−shell radius (nm) | 43.5 | 44.2 | 44.1 | 45.7 | 46.1 |

| sample | p(MA-N) 15 °C | p(MA-N) 30 °C | p(MA-N) 37 °C | p(MA-N) 45 °C |
|---|---|---|---|---|
| core radius $a$ (nm) | 36.7 | 36.7 | 36.7 | 36.7 |
| $SLD_{shell}$ ($cm^{-2}$) | $8.2 \times 10^9$ | $8.8 \times 10^9$ | $9.5 \times 10^9$ | $1.6 \times 10^{10}$ |
| shell thickness $d$ (nm) | 5.9 ± 2.4 | 6.5 ± 2.6 | 8.9 ± 2.8 | 8.2 ± 2.6 |
| $\varphi$ | 1.00 | 0.99 | 0.98 | 0.85 |
| DLS core−shell radius (nm) (volume-average) | 86.5 | 55.5 | 43.5 | 46.5 |
| SANS core−shell radius (nm) | 42.6 | 43.2 | 45.6 | 44.9 |

[a]The derived scattering length density of the shell ($SLD_{shell}$) and polymer volume fraction in the shell ($\varphi$) are also reported. For the sake of comparison, volume-average particle sizes derived from DLS are given. Volume-average core radii were obtained from an analysis of SANS data collected on particles devoid of the shell. For appropriate comparison to SANS, volume-average (and not intensity-average) sizes determined by DLS must be considered. See text and Supporting Information (Part III) for further details.

relevant for data modeling and obtained as explained in Supporting Information.

Let us first comment on the results pertaining to p(N-AA) particles (Figure 5A,B and Table 1). In line with the shift observed for the positions of the intensity minima with increasing $T$, $d$ increases from 6.8 ± 2.3 nm to 9.4 ± 2.6 nm from $T$ = 15 to 45 °C, which corresponds to a volume-average particle radius $r_0 = a + d$ ranging from 43.5 to 46.1 nm in this temperature range. Except at temperatures well beyond the LCST, the SANS-derived particle size is significantly smaller than that obtained from the volume-average DLS radii that vary between 103.5 and 46.5 nm (Table 1) from $T$ = 15 to 45 °C. These results suggest that the shell is organized according to a dense layer detected by SANS and condensed on the core surface, and a larger peripheral shell layer probed by DLS but too dilute to contribute to SANS signal. This is confirmed by SANS data analysis at $T$ = 15 °C where the obtained $SLD_{shell}$ (= $7.1 \times 10^9$ $cm^{-2}$) is very close to the theoretical value predicted for a pure solvent-free PNIPAM shell ($SLD_{shell,\varphi=1} = 7.4 \times 10^9$ $cm^{-2}$, where $\varphi$ is the polymer volume fraction in the particle shell; see details in Supporting Information).

The existence of such a microphase segregated structure with most of the brush in a condensed high-density phase (detected by SANS) and a small fraction in an expanded low-density phase (detected by DLS) supports qualitative conclusions previously obtained from mean-field simulations.[14] Previous molecular dynamic (MD) simulations of polyelectrolyte brushes quantitatively demonstrated the possible existence of such microphase shell separation for spherical polyelectrolyte brushes.[37] Depending on the solvent quality for the polymer backbone and the strength of the electrostatic interactions, MD computations showed indeed that particle-supported brush may adopt a wide range of morphologies, in particular a "star of bundles" conformation where protruding chains self-assemble into clusters of pinned cylindrical micelles that surround a condensed polymer layer at the core surface. This shell segregation, also described by de la Cruz et al.,[38,39] may explain the observed nonapplicability of the conventional swelling power-law $R_H \propto a + (c^\infty)^{-1/3}$ (section 3.1.1). Experimental data further demonstrate that the microphase segregated structure does exist all across the temperature range 15 °C−45 °C, and that the nonideal brush behavior also occurs at room temperature (25 °C), a feature not accounted for in the modeling detailed in ref 14. The remaining issue to clarify is the origin of the increase in the SANS-derived particle size $r_0$ with increasing $T$, though the accompanying collapse of the shell evidenced by DLS should lead to decreasing $r_0$ (Table 1).

The explanation for this intriguing observation is found from careful inspection of the temperature-dependent $SLD_{shell}$ (Table 1). Both shell thickness and $SLD_{shell}$ values obtained from SANS analysis at $T$ = 23 °C are higher than those at 15 °C. This increase in $r_0$ thus stems from the (partial) collapse of the protruding chains on the condensed-high density region supported by the core, which leads to a SANS-detected shell layer containing slightly more solvent (trapped by the partially collapsed chains) compared to the situation at 15 °C. This ultimately results in an increase of $SLD_{shell}$, having in mind that $SLD_{solv} > SLD_{shell,\varphi=1}$ with $SLD_{solv}$ the tabulated scattering length density of the solvent $D_2O$ (see Table S1, Supporting Information). At sufficiently large $T$ above the LCST, the collapse of the peripheral diluted shell layer becomes pronounced (Figure 1D), and water expulsion from the shell is very significant. This explains the decrease of $SLD_{shell}$ with increasing $T$ above 23 °C. At 45 °C, $SLD_{shell}$ reaches a value close to that obtained at 15 °C (Table 1), thus emphasizing that chains in the peripheral dilute shell region are in a complete collapsed state. This is further in agreement with the fact that the value of $r_0$ found at 45 °C from SANS compares remarkably well with that obtained from DLS under similar temperature conditions (see Table 1). The polymer volume fraction $\varphi$ in the shell was further estimated at given temperature $T$ from $SLD_{shell}$ using $\varphi(T) = ((SLD_{shell}(T) - SLD_{solv}(T))/(SLD_{shell}(15\ °C) - SLD_{solv}(T)))$ where we adopted the reference $\varphi$ = 1 at 15 °C, choice motivated by the equality $SLD_{shell}(15\ °C) \sim SLD_{shell,\varphi=1}$. In line with the scenario elaborated above, a densification of the shell layer is found for $T$ in the range 23 to 45 °C. From the obtained $a$ and $d$ dimensions of p(N-AA) (Table 1), we further estimate that the condensed shell volume at 15 °C is ca. 68% of that reached at 45 °C. This conclusion also holds for p(MA-N) particles whose SANS features are detailed below.



DOI: 10.1021/acs.langmuir.5b00530
Langmuir 2015, 31, 4779−4790

The comparison between theoretical and experimental SANS data for p(MA-N) particles is given in Figure 5D and the fitted $SLD_{shell}$ and shell thickness $d$ are detailed in Table 1. Similarly to p(N-AA) particles, the analysis evidences the existence of a high-density layer condensed on the core surface with a thickness that increases with increasing temperature due to collapse of the chains located in the surrounding dilute polymer phase. Quantitatively, $d$ increases from 5.9 ± 2.4 nm to 8.2 ± 2.6 nm with increasing $T$ from 15 to 45 °C. As in the previous situation, there is an excellent agreement between (volume-average) particle sizes derived from DLS and SANS at 45 °C. At fixed $T$, the shell thickness for p(MA-N) is ca. 1 nm lower than that of p(N-AA), which *qualitatively* agrees with the respective positioning of the plots hydrodynamic radii $R_H$ versus temperature displayed for p(MA-N) and p(N-AA) in Figure 1C and D, respectively. Unlike p(N-AA), the SANS-detected shell layer of p(MA-N) contains an increased amount of solvent with increasing $T$, especially from 37 to 45 °C, which is manifested by a significant decrease of the polymer volume fraction $\varphi$ and an increase in $SLD_{shell}$ (Table 1). The noticeable increase of the scattered intensity at large $q$ and at 45 °C could suggest an exchange between atmospheric $H_2O$ and $D_2O$. Without excluding this possibility, we further observe that the hydrodynamic radius $R_H$ of p(MA-N) slightly increases at temperature higher than 35 °C probably due to a loss in the steric stabilization of the particles above the volume phase transition temperature (Figure 1C). Accordingly, the temperature range $T$ > 35 °C could mark the onset of particle coagulation. However, the consequences for the SANS response of p(MA-N) at large $q$ remain unclear as details on the only particle interface and not on the particle size are accessible at such large momentum transfer values. In the Conclusion and Perspectives section that follows, we summarize the basic findings of this work and formulate recommendations to improve theoretical modeling[14] of the nonideal brush behavior evidenced here for p(N-AA) and p(MA-N) particulate systems.

## 4. CONCLUSIONS AND PERSPECTIVES

The swelling behavior of core−shell polymer particles with carboxylate charges preferentially located in the vicinity of the core (p(MA-N)) or at the outer shell periphery (p(N-AA)) is measured by DLS and SANS under a broad range of temperature, salt concentration, and solution pH conditions. In line with expectation, increasing pH, decreasing temperature, and/or electrolyte concentration leads to brush swelling. Shell expansion is most pronounced for particles where charges are preferentially in the outer shell region, and an increase of the lower critical solution temperature is observed with displacing carboxylate charges away from the core surface. Electrokinetics confirm the different pH-mediated swelling in p(MA-N) and p(N-AA) particles and the distinct preferential locations of their carboxylate charges. In agreement with potentiometric titration experiments and swelling data, theoretical analysis of p(MA-N) and p(N-AA) electrophoretic mobility further strongly supports the sluggish dissociation of carboxylate groups embedded within the shell, compared with those distributed at the shell/solution interphase. The corresponding difference in (apparent) dissociation constant is attributed to a distinct hydrophobic/hydrophilic balance of the molecular environment of the carboxylate groups depending on their position across the shell. Comparison between DLS and SANS data finally demonstrates the existence of a microphase segregated shell structure in the temperature range 15 °C−45 °C. Particle shell consists of a high density polymer phase condensed onto the core surface, and a peripheral low-density chains phase which originates the multiresponsive particle swelling detected by DLS. This latter peripheral phase does not, however, contribute to the SANS signal due to its high solvent content.

The results obtained in this work prove the presence of a phase segregated shell structure that was suggested from previous semiquantitative Scheutjens−Fleer self-consistent-field (SF-SCF) modeling of p(MA-N) shell swelling.[14] Data further highlight that such a structure systematically exists for temperatures in the range 15 to 45 °C, a feature that is not well modeled in the mean-field SF-SCF approach of ref 14. Clearly, a successful modeling of the rich nonideal behavior of hydrophobic polyelectrolyte brushes requires a refined molecular shell description to rationalize the necessarily coupled chain swelling and charge ionization process throughout the particle shell compartment. This implies a proper account of the spatial distribution for the density of hydrophobic polymer chains and the additional introduction of a radial dependence for the Flory−Huggins parameter $\chi$ to adequately quantify the local water−chain interactions within the particle shell. This amounts to critically revisit the temperature dependence conventionally adopted for $\chi$ in mean-field approaches.

## ■ ASSOCIATED CONTENT

### Supporting Information

Typical self-consistent field modeling of brush height as a function of ionic strength and pH; electrokinetics of p(N-AA) particles as a function of temperature; details on the constrained procedure adopted for quantitative analysis of SANS data; comparison between SANS data obtained for p(MA-N) and p(N-AA) at 15 °C, 15 mM $NaNO_3$ concentration, and pH 5; and summary of all variables used for SANS data modeling. This material is available free of charge via the Internet at http://pubs.acs.org.

## ■ AUTHOR INFORMATION

### Corresponding Author

*E-mail: jerome.duval@univ-lorraine.fr.

### Notes

The authors declare no competing financial interest.

## ■ ACKNOWLEDGMENTS

J.F.L.D. thanks ILL for beamtime on the D11 SANS instrument. The work further benefited from use of SasView software, originally developed as part of the NSF DANSE project, DMR-0520547, under the name SansView. This work was partially supported by Fundação para a Ciência e a Tecnologia (FCT, Portugal) and COMPETE (FEDER) through project PTDC/CTM-NAN/2354/2012.

## ■ MAIN SYMBOLS AND ABBREVIATIONS

$a$ particle core radius
AA acrylic acid
$c^\infty$ bulk $NaNO_3$ concentration
DLS dynamic light scattering
LCST lower critical solution temperature
MA methacrylic acid
NIPAM *N*-isopropylacrylamide



DOI: 10.1021/acs.langmuir.5b00530
*Langmuir* 2015, 31, 4779−4790

p(MA-N) particles with carboxylate charges preferentially located in the vicinity of the core
p(N-AA) particles with carboxylate charges preferentially located in the outer shell periphery
PMMA poly(methyl methacrylate)
$q$ wave vector transfer or "scattering vector"
$r_0$ particle size radius $a+d$
$R_H$ particle hydrodynamic radius
SANS small angle neutron scattering
SF-SCF Scheutjens–Fleer self-consistent field theory
$SLD_{shell}$ neutron scattering length density of the particle shell compartment
$\alpha$ length that reflects the sharpness in chains density distribution at the particle shell/solution interphase
$\varphi$ polymer volume fraction in the particle shell
$\mu$ particle electrophoretic mobility
$\rho_o$ density of charges in the particle shell
$1/\kappa$ debye layer thickness
$1/\lambda_o$ electroosmotic flow penetration length

## REFERENCES


(1) Suwa, K.; Yamamoto, K.; Akashi, M.; Takano, K.; Tanaka, N.; Kunugi, S. Effects of salt on the temperature and pressure responsive properties of poly(N-vinylisobutyramide) aqueous solutions. *Colloid Polym. Sci.* **1998**, *276*, 529–533.
(2) Kuckling, D.; Vo, C. D.; Wohlrab, S. E. Preparation of nanogels with temperature-responsive core and pH-responsive arms by photocross-linking. *Langmuir* **2002**, *18*, 4263–4269.
(3) Cohen Stuart, M. A.; Huck, W. T. S.; Genzer, J.; Müller, M.; Ober, C.; Stamm, M.; Sukhorukov, G. B.; Szleifer, I.; Tsukruk, V. V.; Urban, M.; Winnik, F.; Zauscher, S.; Luzinov, I.; Minko, S. Emerging applications of stimuli-responsive polymer materials. *Nat. Mater.* **2010**, *9*, 101–113.
(4) Crassous, J. J.; Mihut, A. M.; Dietsch, H.; Pravaz, O.; Ackermann-Hirschi, L.; Hirt, A. M.; Schurtenberger, P. Advanced multiresponsive comploids: from design to possible applications. *Nanoscale* **2014**, *6*, 8726–8735.
(5) Kawauchi, Y.; Kojya, Y.; Yusa, S.-I.; Nakashima, K. Stimuli-induced core-corona inversion of micelles of water soluble poly-(sodium styrene sulfonate)-b-poly(N-isopropyl acrylamide) in response to metal-ion and temperature. *J. Colloid Sci. Biotechnol.* **2014**, *3*, 178–183.
(6) Motornov, M.; Roiter, Y.; Tokarev, I.; Minko, S. Stimuli-responsive nanoparticles, nanogels and capsules for integrated multifunctional intelligent systems. *Prog. Polym. Sci.* **2010**, *35*, 174211.
(7) Parasuraman, D.; Serpe, M. J. Poly (N-isopropylacrylamide) microgels for organic dye removal from water. *ACS Appl. Mater. Interfaces* **2011**, *3*, 27322737.
(8) Van Leeuwen, H. P.; Buffle, J.; Duval, J. F. L.; Town, R. M. Understanding the extraordinary ionic reactivity of aqueous nanoparticles. *Langmuir* **2013**, *29*, 10297–10302.
(9) Pinheiro, J. P.; Moura, L.; Fokkink, R.; Farinha, J. P. S. Preparation and characterization of low dispersity anionic multi-responsive core-shell polymer nanoparticles. *Langmuir* **2012**, *28*, 5802–5809.
(10) Hoare, T.; Mclean, D. Kinetic prediction of functional group distributions in thermosensitive microgels. *J. Phys. Chem. B* **2006**, *110*, 20327–20336.
(11) Hoare, T.; Mclean, D. Multi-component kinetic modeling for controlling local compositions in thermosensitive polymers. *Macromol. Theory Simul.* **2006**, *15*, 619–632.
(12) Kubota, K.; Fujishige, S.; Ando, I. Single-chain transition of poly(N-isopropylacrylamide) in water. *J. Phys. Chem.* **1990**, *94*, 5154–5158.
(13) Pelton, R. H.; Pelton, H. M.; Morphesis, A.; Rowell, R. L. Particle sizes and electrophoretic mobilities of poly(N-isopropylacrylamide) latex. *Langmuir* **1989**, *5*, 816–818.
(14) Alves, S. P. C.; Pinheiro, J. P.; Farinha, J. P. S.; Leermakers, F. A. M. Particles decorated by an ionizable thermoresponsive polymer brush in water: experiments and self-consistent field modeling. *J. Phys. Chem. B* **2014**, *118*, 3192–3206.
(15) Fleer, G. J.; Stuart, M. A. C.; Scheutjens, J. M. H. M.; Cosgrove, T.; Vincent, B. *Polymers at Interfaces*, 1st ed.; Chapman & Hall: London, Great Britain, 1993.
(16) Glasoe, P. K.; Long, F. A. Use of glass electrodes to measure acidities in deuterium oxide. *J. Phys. Chem.* **1960**, *64*, 188–189.
(17) Zhulina, E. B.; Birshtein, T. M.; Borisov, O. V. Theory of ionizable polymer brushes. *Macromolecules* **1995**, *28*, 1491–1499.
(18) Pelton, R. Poly(N-isopropylacrylamide) (PNIPAM) is never hydrophobic. *J. Colloid Interface Sci.* **2010**, *348*, 673–674.
(19) Das, M.; Zhang, H.; Kumacheva, E. Microgels: Old materials with new applications. *Annu. Rev. Mater. Res.* **2006**, *36*, 117–142.
(20) Ohshima, H. Electrophoresis of soft particles. *Adv. Colloid Interface Sci.* **1995**, *62*, 189–235.
(21) Duval, J. F. L.; Gaboriaud, F. Progress in electrohydrodynamics of soft microbial particle interphases. *Curr. Opin. Colloid Interface Sci.* **2010**, *15*, 184–195.
(22) Duval, J. F. L.; Ohshima, H. Electrophoresis of diffuse soft particles. *Langmuir* **2006**, *22*, 3533–3546.
(23) Dukhin, S. S.; Zimmermann, R.; Duval, J. F. L.; Werner, C. On the applicability of the Brinkman equation in soft surface electrokinetics. *J. Colloid Interface Sci.* **2010**, *350*, 1–4.
(24) Ascher, U.; Christiansen, J.; Russel, R. D. Collocation software for boundary value ODE's. *ACM Trans. Math. Software* **1981**, *7*, 209–222.
(25) Duval, J. F. L.; Küttner, D.; Werner, C.; Zimmermann, R. Electrohydrodynamics of soft polyelectrolyte multilayers: point of zero-streaming current. *Langmuir* **2011**, *27*, 10739–10752.
(26) Schönherr, H.; Hruska, Z.; Vancso, G. J. Toward high resolution mapping of functional group. *Macromolecules* **2000**, *33*, 4532–4537.
(27) Song, J.; Duval, J. F. L.; Cohen Stuart, M. A.; Hillborg, H.; Gunst, U.; Arlinghaus, H. F.; Vancso, G. J. Surface ionization state and nanoscale chemical composition of UV-irradiated poly-(dimethylsiloxane) probed by chemical force microscopy, force titration and electrokinetic measurements. *Langmuir* **2007**, *23*, 5430–5438.
(28) Lyklema, J. In *Fundamentals of Interface and Colloid Science*; Academic Press: New York, 1995; Electric Double Layers, Vol. *II*, Chapter 3.
(29) Lyklema, J. In *Fundamentals of Interface and Colloid Science*. Academic Press New York, 1995; Electrokinetics and Related Phenomena, Vol. *II*, Chapter 4.
(30) Catenaccio, A.; Daruich, Y.; Magallanes, C. Temperature dependence of the permittivity of water. *Chem. Phys. Lett.* **2003**, *367*, 669–671.
(31) Kampmeyer, P.M. The temperature dependence of viscosity for water and mercury. *J. Appl. Phys.* **1952**, *23*, 99.
(32) Coury, L. Conductance Measurements. Part 1: Theory. *Curr. Sep.* **1999**, *18:3*, 91–96.
(33) Berezanski, P. In *Handbook of Instrumental Techniques for Analytical Chemistry*; Settle, F., Ed.; Prentice-Hall: Upper Saddle River, NJ, 1997; Chapter 39, pp 749–764.
(34) Martin, J.; Bihannic, I.; Demé, B.; Duval, J. F. L.; Michot, L.; Rotureau, E. *Measurement of Structural Changes in Multi-responsive Core-Shell Polymer Particles*; Institut Laue-Langevin (ILL): Grenoble, 2013; DOI:10.5291/ILL-DATA.9-10-1310.
(35) Guinier, A.; Fournet, G. *Small Angle Scattering of X-Rays*; John Wiley and Sons: New York, 1955.
(36) Grillo, I. In *Small-angle neutron scattering and applications in soft condensed matter*; Borsali, R., Pecora, R., Eds.; Springer: New York, 2008; Volume II, Chapter 13.
(37) Sandberg, D. J.; Carrillo, J.-M. Y.; Dobrynin, A. V. Molecular dynamics simulations of polyelectrolyte brushes: from single chains to bundles of chains. *Langmuir* **2007**, *23*, 12716–12728.
(38) Solis, F. J.; Stupp, S. I.; Olvera de la Cruz, M. Charge induced pattern formation on surfaces: Segregation in cylindrical micelles of



DOI: 10.1021/acs.langmuir.5b00530
*Langmuir* 2015, 31, 4779–4790

cationic-anionic peptide-amphiphiles. *J. Chem. Phys.* **2005**, *122*, 054905.
(39) Loverde, S. M.; Solis, F. J.; Olvera de la Cruz, M. Charged particles on surfaces: coexistence of dilute phases and periodic structures at interfaces. *Phys. Rev. Lett.* **2007**, *98*, 237802.



DOI: 10.1021/acs.langmuir.5b00530
*Langmuir* 2015, 31, 4779−4790